


Topological conditions for impurity effects in carbon nanosystemsYuriy G. Pogorelov ^{*}*IFIMUP-IN, Departamento de Física, Universidade do Porto, Porto 4169-007, Portugal*Vadim M. Loktev[†]*N. N. Bogolyubov Institute of Theoretical Physics, NAS of Ukraine, Kyiv 03134, Ukraine
and Igor Sikorsky Kyiv Polytechnic Institute, Kyiv 03056, Ukraine* (Received 12 December 2023; accepted 7 August 2024; published 22 August 2024)

We consider electronic spectra of carbon nanotubes and their perturbation by impurity atoms absorbed at different positions on nanotube surfaces, within the framework of the Anderson hybrid model. Special attention is given to the cases in which Dirac-like 1D modes appear in the nanotube spectrum and their hybridization with localized impurity states produces, at growing impurity concentration c , onset of a mobility gap near the impurity level and even opening, at yet higher c , of some narrow delocalized range within this mobility gap. Such behaviors are compared with similar effects in the previously studied 2D graphene and armchair-type graphene nanoribbons. Some possible practical applications are discussed.

DOI: [10.1103/PhysRevB.110.075142](https://doi.org/10.1103/PhysRevB.110.075142)**I. INTRODUCTION**

Since the discovery 20 years ago of single-layer graphene [1], there has been much interest not only in its two-dimensionality (2D) [2] but mainly in its massless, that is, Dirac-like, spectrum of electronic excitations [3]. Studies of its various physical properties have a very broad nomenclature [4,5] (see also [6]), but we focus here on certain aspects of nonideal graphene structures, yet restricted to a single dimension (1D), namely, of graphene nanoribbons (NRs) [7] and carbon nanotubes (NTs) [8,9] in the presence of impurities [10–14]. Mostly, we consider here the electron quasiparticle spectra in principal topological types of graphene 1D nanosystems and their restructuring under effects by impurity atoms absorbed at different positions over carbon atoms [15,16]. In this course, the main attention is given to the cases in which Dirac-like 1D modes are present in the NT spectrum [17], and we compare the impurity disorder effects on such modes with those previously studied in 2D graphene [18] and in armchair-type nanoribbons (ANRs) [19]. Also, the specifics of impurity effects in more general twisted carbon NTs are briefly discussed. The main purpose of this analysis is in finding possible practical applications for such 1D-like semimetallic systems under their properly adjusted doping as more compact and sensible analogs for common doped semiconductors.

The presentation is organized as follows. We begin with a description of quasiparticle spectra for two basic NT topologies: zigzag (ZNTs, Sec. II) and armchair (ANTs, Sec. III), in the forms adjusted to describe the impurity-induced restructuring of their spectra. This description, within the simplest T -matrix approximation for the quasiparticle self-energy, begins from the technically simpler ANT case (Sec. IV) and then extends to a more involved ZNT case (Sec. V). The next com-

parison with the previous results for 2D graphene and ANRs (Sec. VI) reveals both qualitative similarities and some quantitative differences in their behaviors. The general topology of twisted nanotubes (TNTs) is discussed in Sec. VII, suggesting a qualitative difference between the twisted and nontwisted NTs in their sensitivity to impurity disorder. The obtained results are then verified with some T -matrix improvements (Sec. VIII): the self-consistent T -matrix method and the group expansion (GE) method, both of them confirming the validity of the simple T -matrix picture. The final discussion of these theoretical results and of some perspectives for their practical applications is given in Sec. IX.

II. ZIGZAG NANOTUBES

Carbon NTs can be obtained from carbon NRs by closure of their edges (for instance, of basic zigzag or armchair types), and these nanotubes are usually classified by the normals to their axes (that is, to the related NR edges). Thus, folding of an armchair nanoribbon (ANR) produces a ZNT and, vice versa, that of a zigzag nanoribbon (ZNR) produces an ANT.

Beginning from the ANR case, it can be seen as a composite of n chains (labeled by j indices) of transversal period a (the graphene lattice constant), each chain containing $N \gg 1$ segments (labeled by p indices) of longitudinal period $a\sqrt{3}$ and each segment including 4 atomic sites (labeled by s indices; see Fig. 1). Next, the closure between the 1st and n th chains of an ANR transforms it into a ZNT (see Fig. 2).

For the following consideration of electronic dynamics, it is suitable to combine the local Fermi operators $a_{p,j,s}$ at 4 s sites from the j th chain in the p th segment into the 4-spinor:

$$a_{p,j} = \begin{pmatrix} a_{p,j;1} \\ a_{p,j;2} \\ a_{p,j;3} \\ a_{p,j;4} \end{pmatrix}. \quad (1)$$

^{*}Contact author: ypogorel@fc.up.pt[†]Contact author: vloktev@bitp.kiev.ua

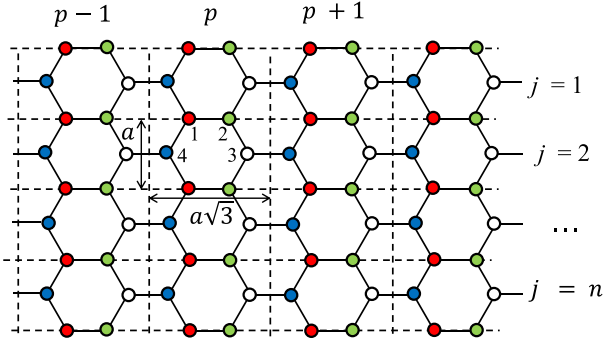


FIG. 1. An armchair nanoribbon composed of n atomic chains (j -labeled), each chain consisting of segments (p -labeled) with 4 atomic sites, $s = 1$ (red), 2 (green), 3 (white), 4 (blue), in each segment.

Then the longitudinal translation invariance (with the $a\sqrt{3}$ period; see Fig. 1) and the discrete transversal rotation invariance of the obtained ZNT suggest the Fourier expansion of the local spinor components in quasicontinuous longitudinal momentum $-\pi/\sqrt{3} < k < \pi/\sqrt{3}$ and in discrete transversal wave number $q = 0, \dots, n-1$ (both in a^{-1} units):

$$a_{p,j,s} = \frac{1}{2\sqrt{nN}} \sum_{k,q} \exp \left[i \left(\sqrt{3}kp_s + \frac{2\pi q}{n} j_s \right) \right] \alpha_{k,q,s}. \quad (2)$$

Its components $\alpha_{k,q,s}$ form the wave spinor $\alpha_{k,q}$. Here the longitudinal numbers for different s sites are $p_{1,2} = p \pm 1/6$, $p_{3,4} = p \pm 1/3$ and their transversal numbers are $j_{1,2} = j$, $j_{3,4} = j + 1/2$. Then the ZNT Hamiltonian taking only account of hopping between nearest-neighbor atoms (its parameter, $t \approx 2.8$ eV [3], taken as the energy scale in what follows) is presented in terms of wave spinors as¹

$$H_{ZNT} = \sum_{k,q} \alpha_{k,q}^\dagger \hat{H}_{k,q} \alpha_{k,q}. \quad (3)$$

Here the 4×4 matrix

$$\hat{H}_{k,q} = \begin{pmatrix} 0 & h_k & 0 & h_{k,q}^* \\ h_k^* & 0 & h_{k,q} & 0 \\ 0 & h_{k,q}^* & 0 & h_k \\ h_{k,q} & 0 & h_k^* & 0 \end{pmatrix} \quad (4)$$

has its elements $h_k = e^{ik/\sqrt{3}}$ and $h_{k,q} = 2e^{ik/2\sqrt{3}} \cos \frac{\pi q}{n}$. The ZNT spectrum results from four eigenvalues of this matrix at given k and q as

$$\begin{aligned} \varepsilon_{k,q;1} &= -\varepsilon_{k,q;2} = -\varepsilon_{k,q}, \\ \varepsilon_{k,q;3} &= -\varepsilon_{k,q;4} = -\varepsilon_{k,n-q}, \end{aligned} \quad (5)$$

with the basic dispersion law

$$\varepsilon_{k,q} = \sqrt{1 + 4 \cos \frac{\sqrt{3}k}{2} \cos \frac{\pi q}{n} + 4 \cos^2 \frac{\pi q}{n}}. \quad (6)$$

¹The common nearest-neighbor hopping approximation stays practically insensitive to the NT curvature at $n \gg 1$ since the distance to next-nearest neighbors there stays to within $\sim 1/n^2$, the same as in 2D graphene.

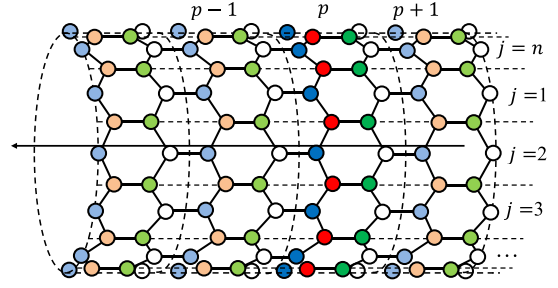


FIG. 2. A zigzag nanotube formed by closing links between the 1st and n th chains of the armchair nanoribbon in Fig. 1.

This can be seen either as the standard graphene dispersion law [20] but with discrete transversal momentum numbers q or, otherwise, as a set of $4n$ 1D k bands $\varepsilon_{k,q;f}$ (for n possible values of q and 4 values of f). Notably, a double degeneracy of these bands follows from Eqs. (5) and (6) as

$$\varepsilon_{k,q;1} \equiv \varepsilon_{k,n-q;3}, \quad \varepsilon_{k,q;2} \equiv \varepsilon_{k,n-q;4}. \quad (7)$$

Thus, if n is even, the ZNT spectrum has 4 nondegenerated (for $q = 0$ and $q = n/2$) modes and $2n - 2$ doubly degenerated ones. Otherwise, if n is odd, there are two nondegenerated modes (only for $q = 0$) and $2n - 1$ doubly degenerated ones. The eigenoperators $\psi_{k,q;f}$ of these modes enter the diagonal ANT Hamiltonian:

$$H = \sum_{k,q,f} \varepsilon_{k,q;f} \psi_{k,q;f}^\dagger \psi_{k,q;f}. \quad (8)$$

These operators at given k and q can also be combined into the 4-spinor $\psi_{k,q}$, related to the α -spinor as

$$\psi_{k,q} = \hat{U}_{k,q} \alpha_{k,q}, \quad (9)$$

through the unitary matrix

$$\hat{U}_{k,q} = \frac{1}{2} \begin{pmatrix} -z_{k,q} & -1 & z_{k,q} & 1 \\ z_{k,q} & -1 & -z_{k,q} & 1 \\ -z_{k,n-q} & 1 & -z_{k,n-q} & 1 \\ z_{k,n-q} & 1 & z_{k,n-q} & 1 \end{pmatrix},$$

with the complex phase factor

$$z_{k,q} = \exp \left[i \left(\frac{k}{\sqrt{3}} + \arctan \frac{\sin \frac{k}{2\sqrt{3}}}{2 \cos \frac{\pi q}{n} - \cos \frac{k}{2\sqrt{3}}} \right) \right].$$

Contrariwise, the α -spinor follows from the ψ -spinor by the inversion of Eq. (9):

$$\alpha_{k,q} = \hat{U}_{k,q}^\dagger \psi_{k,q}. \quad (10)$$

Other important features of the ZNT spectrum by Eq. (5) are

- (i) the presence of 2 flat (dispersionless) modes for even n (then at $q = n/2$) and
- (ii) the presence of 4 gapless Dirac-like modes (DLMs) for n being a multiple of 3 (then at $q = n/3$ and $q = 2n/3$).

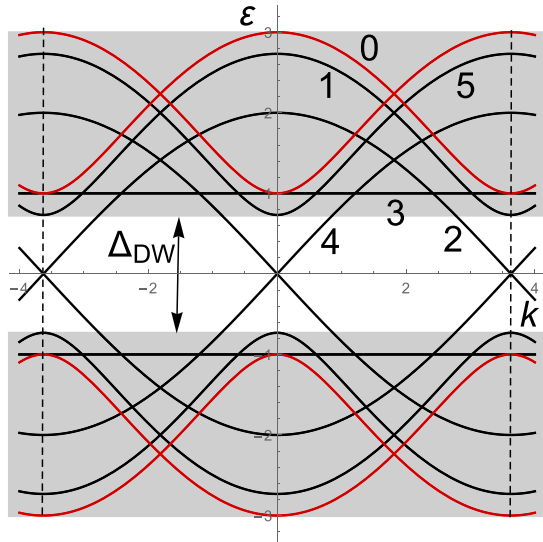


FIG. 3. Dispersion laws for ZNT of $n = 6$ chains, with doubly degenerated (black) and nondegenerated (red) modes; the Dirac window of width $\Delta_{DW} = 2(\sqrt{3} - 1)$ is in between the shaded ranges of the resting modes.

The latter are just the 1D analogs to the 2D graphene Dirac modes with their nodal points K (here at $k = 2\pi/\sqrt{3}$, $q = n/3$) and K' (here at $k = 0$, $q = 2n/3$); also they are fully analogous to DLMs in ANRs [19].

Due to the DLMs' special sensitivity to local impurity perturbations, our following treatment is mainly focused on these modes. In this course, the most relevant energy range is the Dirac window (DW), exclusively occupied with DLMs and delimited by the inner edges of their nearest-neighbor modes (Fig. 3). From Eq. (6), this window results in width

$$\Delta_{DW} = 2 \left| 1 - \cos \frac{\pi}{n} - \sqrt{3} \sin \frac{\pi}{n} \right|, \quad (11)$$

and with growing $n \gg 1$ it is narrowing as $\sim 2\sqrt{3}\pi/n$.

Now, considering the low-energy spectrum range, the expansion of local operators by Eqs. (2) and (10) can be

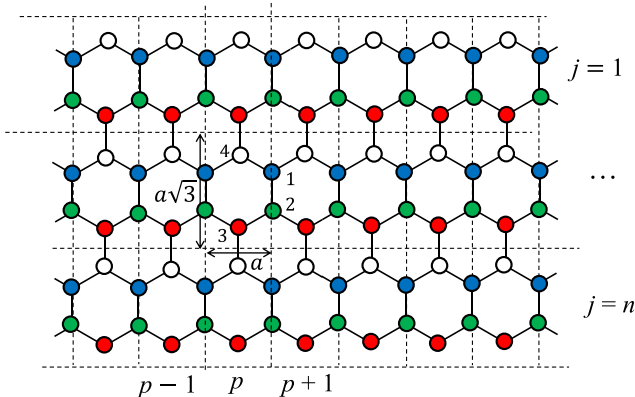


FIG. 4. A zigzag nanoribbon of $j = 1, \dots, n$ chains, with $s = 1$ (blue), 2 (green), 3 (red), and 4 (white) sites in each p th segment.

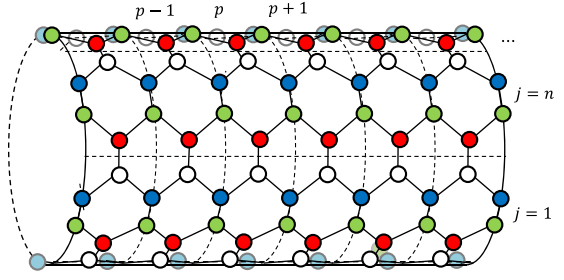


FIG. 5. An n -chain armchair nanotube formed by closure between the 1st and n th chains of zigzag nanoribbon from Fig. 4.

restricted to 8 K, K' DLMs which share 4 eigenenergies:

$$\begin{aligned} \varepsilon_{k,K,1} = -\varepsilon_{k,K,2} = -\varepsilon_{k,K',1} = \varepsilon_{k,K',2} &= 2 \sin \frac{\sqrt{3}k}{4}, \\ \varepsilon_{k,K,3} = -\varepsilon_{k,K,4} = -\varepsilon_{k,K',3} = \varepsilon_{k,K',4} &= 2 \cos \frac{\sqrt{3}k}{4}. \end{aligned} \quad (12)$$

Thus, the restricted expansion of a local spinor in eigen-spinors is presented in the form

$$a_{p,j} = \frac{1}{2\sqrt{nN}} \sum_k e^{i\sqrt{3}kp} \left(e^{i\frac{2\pi}{3}j} U_{k,K}^\dagger \psi_{k,K} + e^{i\frac{4\pi}{3}j} U_{k,K'}^\dagger \psi_{k,K'} \right), \quad (13)$$

including the unitary matrices

$$\begin{aligned} \hat{U}_{k,K} &= \frac{1}{2} \begin{pmatrix} -iz_k & -1 & iz_k & 1 \\ iz_k & -1 & -iz_k & 1 \\ z_k & 1 & z_k & 1 \\ -z_k & 1 & -z_k & 1 \end{pmatrix}, \\ \hat{U}_{k,K'} &= \frac{1}{2} \begin{pmatrix} -z_k & -1 & z_k & 1 \\ z_k & -1 & -z_k & 1 \\ -iz_k & 1 & -iz_k & 1 \\ iz_k & 1 & iz_k & 1 \end{pmatrix} \end{aligned}$$

with $z_k = e^{ik/2\sqrt{3}}$. This expansion is suitable for the following construction of the impurity perturbation Hamiltonian.

III. ARMCHAIR NANOTUBES

For the case of the ANT we also consider its structure obtained from an n -chain ZNR (Fig. 4) by closure between its 1st and n th chains (Fig. 5). Comparison of Fig. 4 with Fig. 1 readily shows that the ANT elementary cell results just from 90° rotation of the ZNT one, so the analysis of ANT spectra simply follows that for ZNT but with the $\sqrt{3}k \longleftrightarrow 2\pi q/n$ interchange. Thus the ANT Hamiltonian in terms of 4-spinor wave operators results, in analogy with the ZNT form by Eq. (2), as

$$H_{ANT} = \sum_{k,q} \alpha_{k,q}^\dagger \hat{H}_{q,k} \alpha_{k,q}, \quad (14)$$

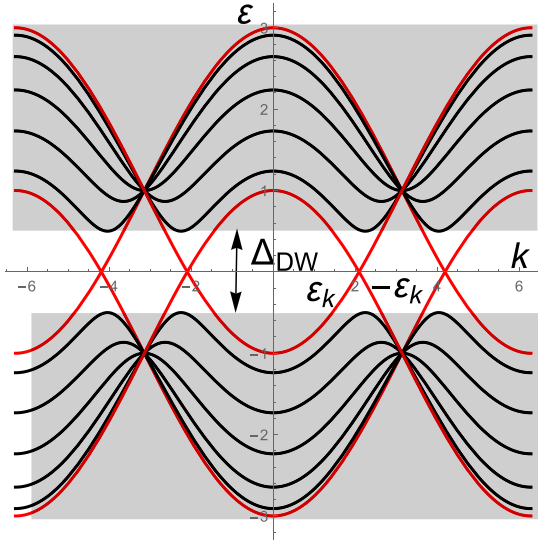


FIG. 6. Dispersion laws for ANT of $n = 6$ chains, with doubly degenerated (black) and nondegenerated (red) modes. The Dirac window of width $\Delta_{\text{DW}} = 1$ is more narrow than for the ZNT in Fig. 3.

where the 4×4 matrix

$$\hat{H}_{q,k} = \begin{pmatrix} 0 & h_q & 0 & h_{q,k}^* \\ h_q^* & 0 & h_{q,k} & 0 \\ 0 & h_{q,k}^* & 0 & h_q \\ h_{q,k} & 0 & h_q^* & 0 \end{pmatrix} \quad (15)$$

has its elements $h_q = e^{i2\pi q/3n}$ and $h_{q,k} = 2e^{i\pi q/3n} \cos k/2$. The ANT spectrum at given k and q results from the indicated interchange in Eqs. (5) and (6) as

$$\varepsilon_{q,k;1} = -\varepsilon_{q,k;2} = -\varepsilon_{q,k}, \quad \varepsilon_{q,k;3} = -\varepsilon_{q,k;4} = -\varepsilon_{-q,k}, \quad (16)$$

where

$$\varepsilon_{q,k} = \sqrt{1 + 4 \cos \frac{\pi q}{n} \cos \frac{k}{2} + 4 \cos^2 \frac{k}{2}}. \quad (17)$$

This spectrum includes the same numbers of nondegenerated and doubly degenerated eigenmodes as in the above considered ZNT case. But it differs from that case by

(i) the absence of flat modes and

(ii) the presence of two Dirac nodal points: $k = 2\pi/3$ (K) and $k = -2\pi/3$ (K') at the same $q = 0$ and for *any* ANT width n value. Notably, the related two DLMs are nondegenerated [compare with Eq. (12)]:

$$\varepsilon_{0,k;3} = -\varepsilon_{0,k;4} \equiv \varepsilon_k = 1 - 2 \cos \frac{k}{2}. \quad (18)$$

For the ANT case (see Fig. 6), the DW width ends up being $\Delta_{\text{DW}} = 2 \sin \pi/n$, that is, narrowing with $n \gg 1$ as $\Delta_{\text{DLM}} \sim 2\pi/n$ [to be compared with the ZNT case by Eq. (11)].

It should be also noted that, unlike a complete similarity between the ZNT and ANR spectra, there is an important difference between those for ANT and ZNR (the latter having no DLMs at all but presenting instead a special edge mode [19,21]).

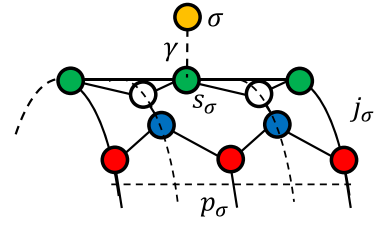


FIG. 7. A fragment of ANT with σ th impurity adatom (orange) linked by hybridization γ to its nearest-neighbor host atom (green) at the $(p_\sigma, j_\sigma, s_\sigma)$ site.

Then the expansion of local operators [an analog to Eq. (13)], reduced to only DLM eigenoperators, results as

$$a_{p,j,s} = \frac{1}{2\sqrt{nN}} \sum_k e^{ikp_s} u_s^\dagger \psi_k, \quad (19)$$

with 2-spinors:

$$\psi_k = \begin{pmatrix} \psi_{0,k;3} \\ \psi_{0,k;4} \end{pmatrix}, \quad u_1 = \begin{pmatrix} -1 \\ 1 \end{pmatrix} = -u_3, \quad u_2 = \begin{pmatrix} -1 \\ -1 \end{pmatrix} = -u_4. \quad (20)$$

Due to the relative simplicity of expansions by Eq. (19) in only 2 DLMs, compared to the ZNT case by Eq. (13) with up to 8 DLMs, we begin the next consideration of impurity effects just from the ANT case.

IV. IMPURITY EFFECTS ON ANT

Now we can consider impurity effects on the above described NTs. The simplest Lifshitz isotopic perturbation model [22] is known not to produce impurity resonance effects in NRs, neither in ANRs or ZNRs [19]; therefore we begin from the more effective Anderson hybrid model [23], presenting its perturbation Hamiltonian for the ANT case [with use of 2-spinors by Eq. (19)] as

$$H_{\text{AZ}} = \sum_\sigma \left[\varepsilon_{\text{res}} b_\sigma^\dagger b_\sigma + \frac{\gamma}{2\sqrt{nN}} \sum_k (e^{ikp_\sigma} b_\sigma^\dagger u_{s_\sigma}^\dagger \psi_k + \text{H.c.}) \right]. \quad (21)$$

It describes impurity adatoms with their resonance energy ε_{res} (laying inside the host DLM range) and corresponding local Fermi operators b_σ at random positions σ , linked through the hybridization parameter γ to its nearest-neighbor host atom at the s_σ site in the p_σ segment of the j_σ chain (see Fig. 7). The random p_σ, j_σ , and s_σ values are distributed uniformly with a low overall concentration: $c = (4nN)^{-1} \sum_\sigma 1 \ll 1$.

The next consideration goes in terms of (advanced) Green's functions (GFs) whose Fourier transform in energy

$$\langle\langle A|B \rangle\rangle_\varepsilon = \frac{i}{\pi} \int_{-\infty}^0 e^{i(\varepsilon-i0)t} \langle\langle A(t), B(0) \rangle\rangle dt \quad (22)$$

includes the grand-canonical statistical average $\langle O \rangle = \text{Tr} [e^{-(H-\mu)/k_B T} O_H(t)] / \text{Tr} [e^{-(H-\mu)/k_B T}]$ of a Heisenberg operator $O(t) = e^{iHt} O e^{-iHt}$ under a Hamiltonian H with chemical potential μ and the anticommutator $\{\cdot, \cdot\}$.

As known [24,25], GFs satisfy the equation of motion:

$$\varepsilon \langle\langle A|B \rangle\rangle_{\varepsilon} = \langle\{A(0), B(0)\}\rangle + \langle\langle [A, H]|B \rangle\rangle_{\varepsilon}. \quad (23)$$

In what follows the energy subindex at GFs is mostly omitted (or enters directly as its argument).

Consider now the GF 2×2 matrix $\hat{G}(k, k') = \langle\langle \psi_k | \psi_{k'}^{\dagger} \rangle\rangle$ made of ψ -spinors by Eq. (19). In the absence of impurities, with the use of the Hamiltonian H by Eq. (3), the explicit solution for this GF turns k -diagonal: $\hat{G}(k, k') \rightarrow \delta_{k,k'} \hat{G}^{(0)}(k)$, where

$$\hat{G}_0(k) = (\varepsilon - \varepsilon_k \hat{\tau}_3)^{-1} \quad (24)$$

with the Pauli matrix $\hat{\tau}_3$.

When passing to the disordered system with its Hamiltonian extended to $H + H_{AZ}$, we get the equation of motion for the k -diagonal GF matrix, $\hat{G}(k, k) \equiv \hat{G}(k)$,

$$\hat{G}(k) = \hat{G}_0(k) + \frac{\gamma}{2\sqrt{nN}} \sum_{\sigma} e^{-ik'p_{\sigma}} \hat{G}_0(k) u_{s_{\sigma}} \langle\langle b_{\sigma} | \psi_k^{\dagger} \rangle\rangle, \quad (25)$$

and then its solution is generally sought in the self-energy form,

$$\hat{G}(k) = (\hat{G}_0^{-1}(k) - \hat{\Sigma}_k)^{-1}, \quad (26)$$

including the self-energy matrix $\hat{\Sigma}_k$. To find it, we continue the chain of equations of motion, now for the mixed (impurity-DLM) row-vector GF:

$$\langle\langle b_{\sigma} | \psi_k^{\dagger} \rangle\rangle (\varepsilon - \varepsilon_{\text{res}}) = \frac{\gamma}{2\sqrt{nN}} \sum_{k'} e^{ik'p_{\sigma}} u_{s_{\sigma}}^{\dagger} \hat{G}(k', k). \quad (27)$$

This gives the first contribution to $\hat{\Sigma}_k$ from its term with $k' = k$ used in Eq. (25):

$$\frac{\gamma^2}{4nN} \sum_{\sigma} \frac{u_{s_{\sigma}} u_{s_{\sigma}}^{\dagger}}{\varepsilon - \varepsilon_{\text{res}}} = \frac{c\gamma^2}{\varepsilon - \varepsilon_{\text{res}}}. \quad (28)$$

It is then extended by writing down the equation of motion for the resting terms with $k' \neq k$ on the right-hand side of Eq. (27),

$$\hat{G}(k', k) = \frac{\gamma}{2\sqrt{nN}} \sum_{\sigma'} e^{-ik'p_{\sigma'}} \hat{G}_0(k') u_{s_{\sigma'}} \langle\langle b_{\sigma'} | \psi_k^{\dagger} \rangle\rangle, \quad (29)$$

and choosing the term with $\sigma' = \sigma$ on its right-hand side. This generates the (scalar) impurity self-energy $\Sigma_0 = \gamma^2 G_0$ with the DLM locator GF:

$$G_0 = \frac{1}{4nN} \sum_k u_{s_{\sigma}}^{\dagger} \hat{G}_0(k) u_{s_{\sigma}} = \frac{1}{4nN} \sum_k \text{Tr} \hat{G}_0(k), \quad (30)$$

which enters the modified factor $(\varepsilon - \varepsilon_{\text{res}} - \Sigma_0)$ in Eq. (27). Then the solution for $\hat{G}(k)$ in the simplest T -matrix approximation for self-energy reads

$$\hat{G}(k) = [\varepsilon - cT(\varepsilon)\hat{\tau}_0 - \varepsilon_k \hat{\tau}_3]^{-1}, \quad (31)$$

with the scalar T matrix

$$T(\varepsilon) = \frac{\gamma^2}{\varepsilon - \varepsilon_{\text{res}} - \Sigma_0}. \quad (32)$$

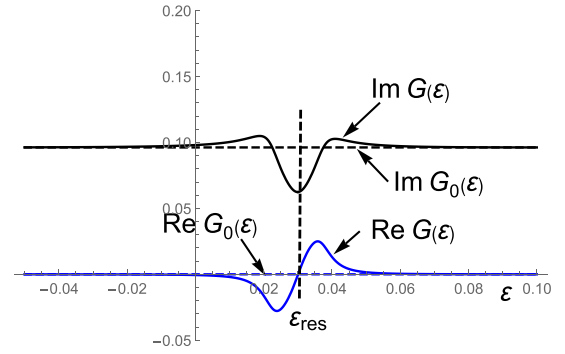


FIG. 8. Real (blue) and imaginary (black) parts of the locator function $G(\varepsilon)$ compared to those by the unperturbed $G_0(\varepsilon)$ (dashed) for ANT with $n = 12$ at Cu impurity concentration $c = 0.08$.

The next important GF, the DLM locator, is calculated by the usual passing from k summation to integration:

$$G_0(\varepsilon) = \frac{\varepsilon}{4n\pi} \int_0^{2\pi} \frac{dk}{\varepsilon^2 - \varepsilon_k^2}. \quad (33)$$

Its analytic expression (see Appendix) is

$$G_0(\varepsilon) = \frac{i}{4n} \left\{ \frac{\theta[(1-\varepsilon)(3+\varepsilon)]}{\sqrt{(3+\varepsilon)(1-\varepsilon)}} + \frac{\theta[(1+\varepsilon)(3-\varepsilon)]}{\sqrt{(3-\varepsilon)(1+\varepsilon)}} \right\}, \quad (34)$$

approximated in the low-energy range as

$$G_0(\varepsilon) \approx \frac{i}{2n\sqrt{3}} \left(1 + \frac{\varepsilon^2}{3} \right). \quad (35)$$

More generally, the DLM locator is defined as

$$G(\varepsilon) = \frac{1}{4\pi N} \sum_k \text{Tr} \hat{G}(k), \quad (36)$$

with the diagonal GF matrix $\hat{G}(k)$ by Eq. (26). Within the T -matrix approximation by Eq. (31), it results simply as

$$G(\varepsilon) = G_0(\tilde{\varepsilon}), \quad (37)$$

with $\tilde{\varepsilon} = \varepsilon - cT(\varepsilon)$ used instead of ε in Eqs. (34) or (35). The resulting $G(\varepsilon)$ real and imaginary parts as shown in Fig. 8 for the choice of Cu impurities with $\varepsilon_{\text{res}} = 0.03$, $\gamma = 0.3$ [26], and $c = 0.08$ only slightly differ from those for unperturbed $G_0(\varepsilon)$ within the $|\varepsilon - \varepsilon_{\text{res}}| \lesssim \gamma^2 |G_0|$ range.

Another set of elementary excitations in the disordered system, that due to impurity atoms, defines the impurity locator GF, $G_{\text{imp}} = N^{-1} \sum_{\sigma} \langle\langle b_{\sigma} | b_{\sigma}^{\dagger} \rangle\rangle$, and its solution in the same approximation reads

$$G_{\text{imp}}(\varepsilon) = cT(\varepsilon)/\gamma^2. \quad (38)$$

Together, the DLM and impurity locators, Eqs. (37) and (38), define the low-energy density of states (DOS) as $\rho(\varepsilon) = \rho_h(\varepsilon) + \rho_{\text{imp}}(\varepsilon)$ with its host and impurity parts:

$$\rho_h(\varepsilon) = \frac{2}{\pi} \text{Im} G(\varepsilon), \quad \rho_{\text{imp}}(\varepsilon) = \frac{2}{\pi} \text{Im} G_{\text{imp}}(\varepsilon) \quad (39)$$

(taking account of 2 spin values).

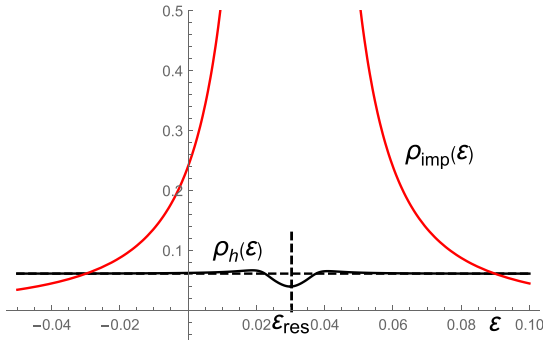


FIG. 9. DOS parts near the impurity resonance level for the same system as in Fig. 8.

In a disordered ANT, host DLMs contribute with $1/n$ charge carriers per site and impurities do with c carriers per site, so defining the Fermi level ε_F from the equation

$$\frac{1}{n} + c = \int_{-3}^{\varepsilon_F} \rho(\varepsilon) d\varepsilon \quad (40)$$

(integrated from the bottom of DLM range). Then, in the simplest approximation of $\text{Im}G(\varepsilon) \approx \text{Im}G_0(\varepsilon) \approx 2/(\sqrt{3}\pi n)$ (dashed line in Fig. 9), the Fermi level dependence on impurity concentration c results:

$$\varepsilon_F(c) \approx \frac{c}{c + c_*} \varepsilon_{\text{res}}, \quad (41)$$

where $c_* = [\gamma G_0(\varepsilon_{\text{res}})]^2$. Its fast initial growth, $\varepsilon_F(c) \approx (c/c_*)\varepsilon_{\text{res}}$ at $c \lesssim c_*$, changes to a slow approach of ε_{res} , $\varepsilon_F(c) \approx \varepsilon_{\text{res}} - (c_*/c)\varepsilon_{\text{res}}$ at $c \gtrsim c_*$ (see Fig. 10).

The next analysis of low-energy spectra in this disordered system follows the lines of similar cases by Refs. [19,27,29]. Thus, the modified dispersion laws are obtained from the standard equation [30],

$$\text{Re det } \hat{G}^{-1}(k) = 0, \quad (42)$$

which splits into two scalar equations,

$$\varepsilon - c \text{Re } T(\varepsilon) = \pm \varepsilon_k. \quad (43)$$

They appear as cubic equations for energy as the function of momentum, $\varepsilon(k)$, and their analytic solutions, though standard, are rather cumbersome. But they can be greatly

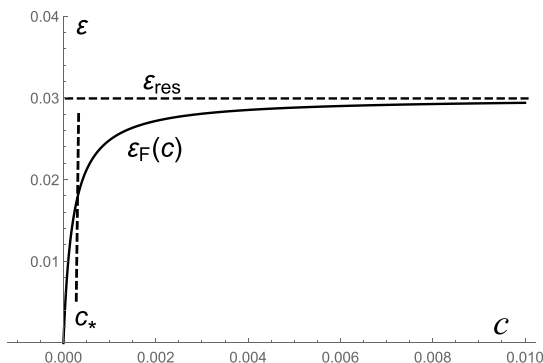


FIG. 10. Fermi level in function of impurity concentration for the system by Figs. 8 and 9.

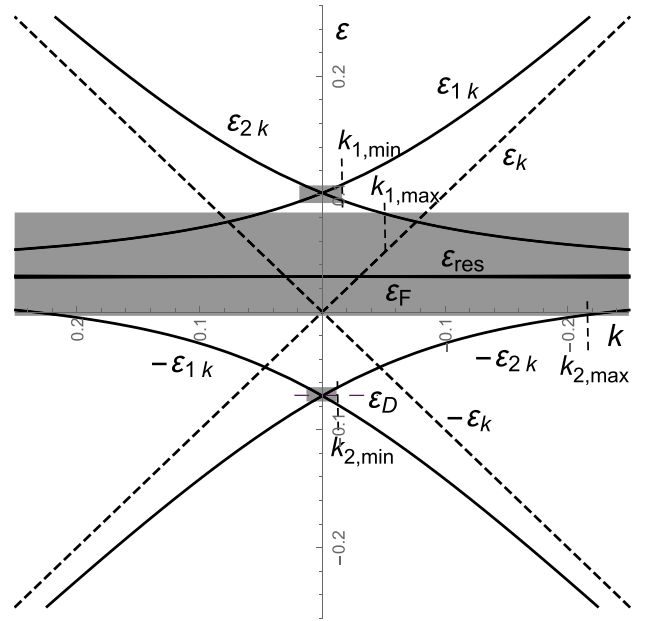


FIG. 11. Modified dispersion laws $\varepsilon_{1,k}$ and $\varepsilon_{2,k}$ by Eq. (45) for the system as in Figs. 8–10 compared to the unperturbed ε_k and to the impurity level ε_{res} (the momentum k being referred to the K point). The mobility gaps (shaded) define the mobility edges $k_{1,\text{min}}$, $k_{2,\text{min}}$, and $k_{2,\text{max}}$ for quasiparticle momenta.

simplified within the relevant low-energy range by using the linearized dispersion law,

$$\varepsilon_k \approx \frac{\sqrt{3}}{2} k, \quad (44)$$

with momentum k referred to the Dirac point and Fermi velocity $\sqrt{3}/2$, and solving Eq. (43) for this momentum as a function of energy [19],

$$\pm k_\varepsilon = \pm 2 \frac{\varepsilon - c \text{Re } T(\varepsilon)}{\sqrt{3}}. \quad (45)$$

An example of such solutions for ANT with $n = 12$ and $c = 0.08$ in Fig. 11 demonstrates how coupling of each $\pm \varepsilon_k$ mode to the impurity ε_{res} mode forms resonance splitting of hybridized $\pm \varepsilon_{1k}$ and $\pm \varepsilon_{2k}$ modes at $k = 0$ to the interval of $\approx \sqrt{\varepsilon_{\text{res}}^2 + 4c\gamma^2}$ around $\varepsilon_{\text{res}}/2$.

Next, this k_ε -form is used in the important test of dispersion law validity for a disordered system, the Ioffe-Regel-Mott (IRM) criterion [31,32],

$$k_\varepsilon v_\varepsilon \gtrsim \tau^{-1}(\varepsilon), \quad (46)$$

with the quasiparticle group velocity $v_\varepsilon = (\partial k_\varepsilon / \partial \varepsilon)^{-1}$ and its inverse lifetime $\tau_\varepsilon^{-1} = c \text{Im } T(\varepsilon)$, that is, the quasiparticle mean free path being longer than its wavelength.

Each ε value that converts \gtrsim into \approx in Eq. (46) gives an estimate for a mobility edge ε_{mob} , separating the ranges of bandlike and localized states in the spectrum. An important rule for these states in a multimode system is that they cannot coexist; that is, if, for a certain energy, the IRM criterion does not hold for at least one mode, all other modes at this energy should be also localized [32].

With use of Eqs. (45) and (32), such equation for mobility edges can be written explicitly in the form

$$\frac{c\gamma^2\Gamma}{D^2(\varepsilon)} \left| 1 + c\gamma^2 \frac{D^2(\varepsilon) - 2\Gamma^2}{D^4(\varepsilon)} \right| \approx \left| \varepsilon - c\gamma^2 \frac{\varepsilon - \varepsilon_{\text{res}}}{D^2(\varepsilon)} \right| \quad (47)$$

with $D^2(\varepsilon) = (\varepsilon - \varepsilon_{\text{res}})^2 + \Gamma^2$ and $\Gamma = \gamma^2 G_0(\varepsilon)$. Then, using the $G_0(\varepsilon)$ value by Eq. (34), this equation can be solved numerically to estimate all possible ε_{mob} values and so delimit the bandlike and localized energy ranges in ZNT with impurities at given disorder parameters (ε_{res} , γ , c) and of NT structure (n) as shown in Fig. 11.

Here one localized range is found at the lower limit of resonance splitting, near the shifted Dirac energy $-\varepsilon_s$ at all $c > 0$, being of width $\approx c\gamma^2/\varepsilon_{\text{res}}$. Another localized range emerges above it, around ε_{res} , when c reaches a certain critical value c_0 . And at yet higher critical concentration, $c_1 \gg c_0$, the latter range gets split in two, due to a specific interplay (when going away from the Dirac point) between the growing momentum k_ε , decreasing group velocity v_k , and increasing inverse lifetime τ_ε^{-1} of hybridized modes. A more detailed description of these restructured spectra for different nanostructures follows below.

V. IMPURITY EFFECTS ON ZNT

It is also of interest to extend the above approach to another NT topology, namely, to the more involved ZNT case. To simplify description of low-energy impurity resonances here, we again restrict the expansions of local operators by Eqs. (2) and (9) in 4-spinors $\psi(k, q)$ with unitary matrices $\hat{U}(k, q)$, to only DLMs $q = K, K'$. Then the ZNT perturbation Hamiltonian results, instead of Eq. (21) for ZNT, in the form

$$\begin{aligned} H_Z = & \sum_{\sigma} \varepsilon_{\text{res}} b_{\sigma}^{\dagger} b_{\sigma} + \frac{\gamma}{2\sqrt{nN}} \sum_{k,\sigma} (e^{ikp_{\sigma}} b_{\sigma}^{\dagger} \\ & \times \{e^{iKj_{\sigma}} [u^{\dagger}(k, K; \sigma) \psi(k, K)]_{j_{\sigma}} \\ & + e^{iK'j_{\sigma}} [u^{\dagger}(k, K'; \sigma) \psi(k, K')]_{j_{\sigma}}\} + \text{H.c.}), \end{aligned} \quad (48)$$

where the row spinor $u^{\dagger}(k, q; \sigma)$ is just the j_{σ} th row of $\hat{U}^{\dagger}(k, q)$.

Next we consider the 4×4 GF matrices $\hat{G}(k, q; k', q') \equiv \langle\langle \psi_{k,q} | \psi_{k',q'}^{\dagger} \rangle\rangle$ and the related equation of motion with the Hamiltonian $H + H_Z$ for the choice of K -mode GF:

$$\begin{aligned} \hat{G}(k, K; k', K) = & \delta_{k,k'} \hat{G}^{(0)}(k, K) + \frac{\gamma}{2\sqrt{nN}} \\ & \times \sum_{\sigma} e^{-i(kp_{\sigma} + Kj_{\sigma})} \hat{G}_0(k, K) \\ & \times u(k, K; \sigma) \langle\langle b_{\sigma} | \psi_{k',K}^{\dagger} \rangle\rangle, \end{aligned} \quad (49)$$

where $G_{f,f'}^{(0)}(k, K) = \delta_{f,f'}(\varepsilon - \varepsilon_{k,K,f})^{-1}$ and the column spinor $u(k, q; \sigma)$ is the j_{σ} th column of $\hat{U}(k, q)$.

Then the equation [similar to Eq. (27) for the ZNT case] for the mixed GF, $\langle\langle b_{\sigma} | \psi_{k',K}^{\dagger} \rangle\rangle$,

$$\begin{aligned} \langle\langle b_{\sigma} | \psi_{k',K}^{\dagger} \rangle\rangle (\varepsilon - \varepsilon_{\text{res}}) = & \frac{\gamma}{2\sqrt{nN}} \sum_{k''} e^{i(k''p_{\sigma} + K'j_{\sigma})} u^{\dagger}(k'', K; \sigma) \\ & \times \hat{G}(k'', k'), \end{aligned} \quad (50)$$

leads [in the same way as to Eq. (31)] to the T -matrix solution for momentum-diagonal GF matrix $\hat{G}(k, K) \equiv \hat{G}(k, K; k, K)$,

$$\hat{G}(k, K) = \{[\hat{G}^{(0)}(k, K)]^{-1} - cT(\varepsilon)\}^{-1}, \quad (51)$$

where the T function for this case differs from that by Eq. (32) only by the form of its locator $G_0(\varepsilon)$. Using Eq. (12), it results here as

$$G_0(\varepsilon) = \frac{4i}{n\sqrt{1 - (\varepsilon/2)^2}}. \quad (52)$$

Then comparison with Eq. (34) shows that the impurity level damping for this case turns $\approx 8\sqrt{3}$ times stronger than for ANT at the same n number, mostly due to the above indicated greater relative weight of DLMs in ZNT than in ANT spectra. This produces strongly different behaviors of IRM mobility edges and qualitatively different structures of localized and bandlike spectra in these two nanosystems.

VI. COMPARISON WITH OTHER CARBON NANOSYSTEMS

The low-energy spectrum restructuring under impurity disorder effect is suitably illustrated by a diagram of mobility edges ε_{mob} between the localized and bandlike energy ranges in function of impurity concentration c . Such diagrams in Fig. 12 permit one to compare the effects of Cu impurities on Dirac modes in the previously considered 2D graphene [29] and ANRs [19] together with the above obtained results for ZNT and ANT.

Some general features, noted for the ANT case, are observed in all of them:

- (i) the formation of a localized range (mobility gap) around the resonance level ε_{res} , at reaching a certain critical concentration c_0 ;
- (ii) the presence of another localized range around the shifted down Dirac level ε_D , being mostly narrower but existing at all $c > 0$;
- (iii) the opening, at a certain higher critical concentration $c_1 \gg c_0$, of a narrow band range within the ε_{res} -related mobility gap.

But this comparison also reveals notably different sensitivity of the corresponding DLMs to the impurity resonance level, depending both on their topological properties (absence or presence of edges and the edge types) and on discrete transversal numbers of chains in a system. Within the IRM formalism, for given impurity parameters ε_{res} and γ , it depends on the host system through its locator function $G_0(\varepsilon)$, like those by Eqs. (34) and (52). This can be further compared with the previously found $G_0(\varepsilon)$ values for 2D graphene, $\varepsilon/\sqrt{3}$ [18], and for ANR with M carbon chains, $4/(M+1)$ [19].

Thus, the impurity-induced localization first occurs at an energy very close to ε_{res} and the related critical concentration c_0 can be estimated from Eq. (47) by setting $\varepsilon = \varepsilon_{\text{res}}$ there. It results generally in

$$c_0 = \frac{[\gamma G_0(\varepsilon_{\text{res}})]^2}{2} \left[1 + \sqrt{1 + 4 \frac{\varepsilon_{\text{res}}}{\gamma^2 G_0(\varepsilon_{\text{res}})}} \right], \quad (53)$$

and for the instance of ANT with $n = 12$ it gives $c_0 \approx 1.7 \times 10^{-4}$ in a reasonable agreement with the numerical calculation

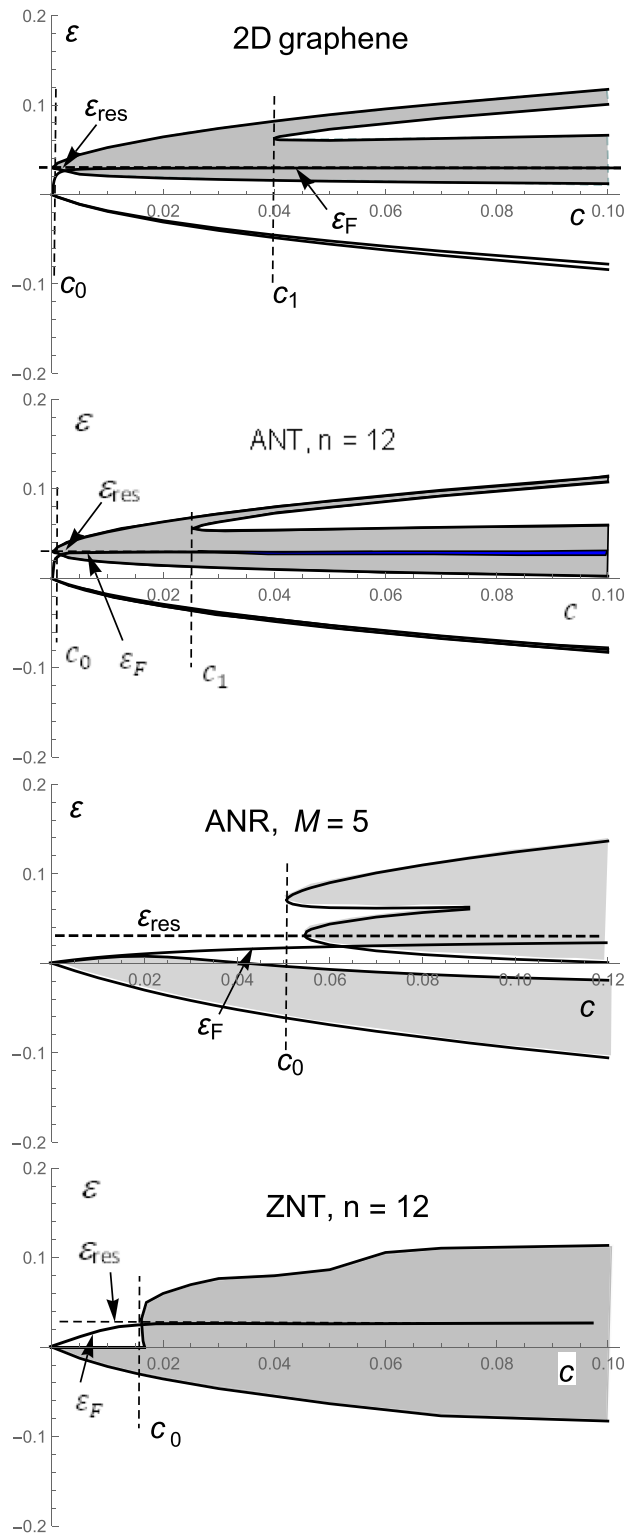


FIG. 12. Development of localized ranges (shadowed) in quasi-particle spectra of 2D graphene, armchair nanotube (with a narrow blue range of divergence for GF group expansion; see Sec. VIII), armchair nanoribbon, and zigzag nanotube with growing Cu impurity concentration.

result shown in Fig. 12. With further growth of $c > c_0$, a continuous range of localized states (mobility gap) appears around ε_{res} , of width growing as $\Delta_{\text{mob}} \sim \gamma\sqrt{c - c_0}$.

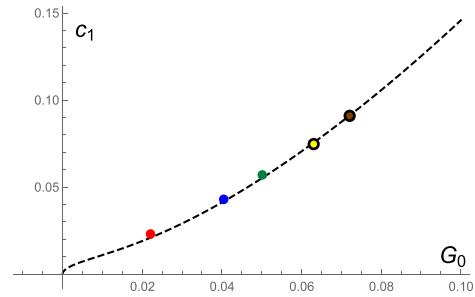


FIG. 13. Upper critical concentration c_1 for Cu impurities in ZNT with $n = 50$ (brown), ANR with $M = 47$ (yellow), ANT with $n = 6$ (green), 2D graphene (blue), and ANT with $n = 12$ (red), together with the fitting curve by Eq. (54) in function of locator G_0 value.

Then, at reaching another critical concentration $c_1 \gg c_0$, a certain window of bandlike states opens inside the mobility gap, due to the before discussed faster resonance splitting between the initial ε_k and ε_{res} modes than these split modes damping. This c_1 value is also estimated from the numerical solution of IRM Eq. (46). It can be presented as a function of the single G_0 parameter as shown in Fig. 13. Strictly speaking, this is only possible for 1D nanosystems where the low-energy locator $G_0(\varepsilon)$ is practically constant, defined by their topology and discrete width numbers. This dependence can be reasonably fitted by the formula

$$c_1 \approx \sqrt{0.01G_0 + 20G_0^3}. \quad (54)$$

The IRM test also indicates a similar mobility window to open under the same impurities in 2D graphene with linear $G_0(\varepsilon)$ behavior. The resulting c_1 value qualitatively agrees with the approximation by Eq. (54) at the choice of $G_0 = G_0(\varepsilon_{op})$, ε_{op} being just the energy where the mobility window first opens (as included in Fig. 13).

Notably, the G_0 parameter decreases with the nanotube width as $\sim 1/n$, producing respective decrease of c_1 and so making the system spectrum more sensible to impurity resonances. Thus, the c_1 value for ZNT with $n > 8$ should turn already below of that for 2D graphene (despite that the latter could be formally thought as the $n \rightarrow \infty$ limit), underlying the importance of topological factors in these effects.

However, as was already noted above, such widening of a nanotube would produce a similar narrowing of the Dirac window Δ_{DW} in its spectrum, delimiting the range of possible impurity effects. Therefore, the optimal conditions for them should be sought from a certain compromise between the parameters of impurity (energy level ε_{res} , hybridization γ , and concentration c) and of host NT (topological type and width n). Thus, for the considered Cu impurities, we estimate admissible width limits for ANT: $n \lesssim 40$, ZNT: $n \lesssim 60$, and ANR: $M \lesssim 35$. Their comparison with the c_1 estimates in Fig. 13 suggests the possibility for the narrow conductivity window above ε_{res} in ANT, graphene, and maybe in ZNT, but hardly in ANR (though the latter can provide a similar window below ε_{res}).

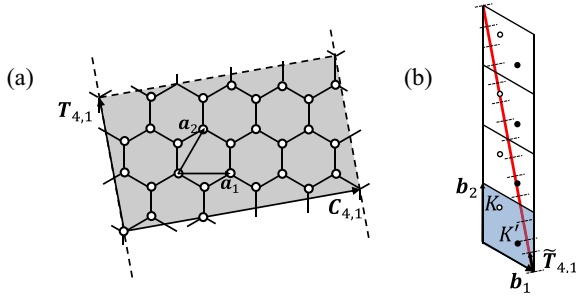


FIG. 14. (a) The unit cell of $n = 4$, $m = 1$ TNT (unfolded) with its chiral $\mathbf{C}_{4,1}$ and longitudinal $\mathbf{T}_{4,1}$ base vectors, containing $N_{4,1} = 28$ atomic positions. (b) The sequence of 14 1D Brillouin zones by this TNT (red line) along the base vector $\tilde{\mathbf{T}}_{4,1} = 2\pi\mathbf{T}_{4,1}/T_{4,1}^2$; it matches certain Dirac points from multiples of 2D graphene BZ (shaded) with its base vectors $\mathbf{b}_{1,2}$, exactly at $2/3$ or $1/3$ of the $\tilde{T}_{4,1}$ periods (dotted segments).

VII. TWISTED NANOTUBES

Yet more general structure of a TNT is intermediate between the above considered ANT and ZNT, with its unit cell being defined by two natural numbers n and m , based on the chiral vector $\mathbf{C}_{n,m} = n\mathbf{a}_1 + m\mathbf{a}_2$ and its orthogonal longitudinal vector $\mathbf{T}_{n,m} = [(2m+n)\mathbf{a}_1 - (2n+m)\mathbf{a}_2]/R_{n,m}$ (where $R_{n,m}$ is the greatest common divisor of $2m+n$ and $2n+m$). There are altogether $N_{n,m} = 4C_{n,m}T_{n,m}/(\sqrt{3}a^2)$ atomic positions in this cell, as shown for the example of $n = 4$, $m = 1$ in Fig. 14(a).

TNT structure differs qualitatively from the limiting ANT and ZNT ones in that it has a single period along $\mathbf{C}_{n,m}$ but repeated periods along the longitudinal $\mathbf{T}_{n,m}$, defining purely 1D translational symmetry. The resulting spectrum consists of $N_{n,m}$ purely 1D modes and it contains DLMs under the condition of $n - m = 3l$ with a natural l [35] (which passes to ANT at $l = 0$ and ZNT at $m = 0$). Then multiple 1D Brillouin zones (BZs) in such a NT with their longitudinal period $\tilde{T}_{n,m} = 2\pi/T_{n,m}$ result just commensurable with the Dirac points in multiple 2D BZs of planar graphene. An example of TNT with $n = 4$, $m = 1$ in Fig. 14(b) shows such matching of its 1D BZs to some of graphene Dirac points.

A treatment of impurity effects on TNT can be done within the above restriction to only DLMs with its results mostly defined by the related value of locator G_0 . But here Eq. (33) should be modified by changing the $4n$ factor to (possibly much bigger) $N_{n,m}$ and also the Fermi velocity $\sqrt{3}/2$ in Eq. (44) to a much higher $T_{n,m}\sqrt{3}/2$, resulting in much lower G_0 values. Then, in accordance with the results of Sec. VI, much lower critical impurity concentrations and much higher sensitivity of (properly chosen) TNT to impurity effects can be expected. A more detailed discussion of these issues will be given elsewhere.

VIII. BEYOND T -MATRIX APPROXIMATION

Besides the most common approach to spectra of disordered systems through the single-impurity scattering in terms of the T matrix, there are its certain extensions. One of them uses the self-consistent approximation to this T matrix [33];

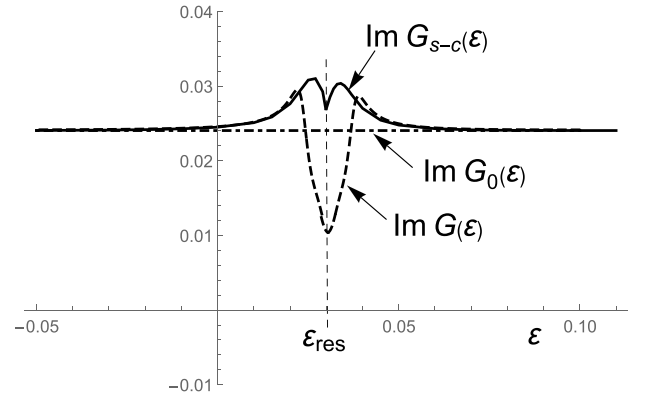


FIG. 15. Imaginary parts of locator functions: self-consistent $G_{s-c}(\epsilon)$ (solid), simple T matrix $G(\epsilon)$ (dashed), and unperturbed $G_0(\epsilon)$ (dash-dotted) for the ANT system as in Figs. 8–11, mostly differing near the resonance level ϵ_{res} .

another is based on group expansions of self-energy [27,28] in series of terms corresponding to wave scatterings by various clusters of increasing number of impurities.

A. Self-consistent approximation

Let us begin from the self-consistent approximation where the T matrix is written as

$$T_{s-c}(\epsilon) = \frac{\gamma^2}{\epsilon - \epsilon_{\text{res}} - \gamma^2 G_{s-c}(\epsilon)}, \quad (55)$$

with the self-consistent locator $G_{s-c}(\epsilon) = G_0[\epsilon - cT_{s-c}(\epsilon)]$.

Then, using the above approximated expression by Eq. (35), we obtain the self-consistency equation for $G_{s-c}(\epsilon)$:

$$i\sqrt{3}n G_{s-c}(\epsilon) + 1 + \frac{1}{3} \left[\epsilon - \frac{c\gamma^2}{\epsilon - \epsilon_{\text{res}} - \gamma^2 G_{s-c}(\epsilon)} \right]^2 = 0. \quad (56)$$

Its numerical solution for the characteristic case of ANT with $n = 6$ and $c = 0.015$ provides the real and imaginary parts by $G_{s-c}(\epsilon)$ as shown in Fig. 15 in comparison with the same parts of the simple $G_0(\epsilon)$, Eq. (32). It demonstrates that the self-consistency correction only slightly changes $G_0(\epsilon)$ in the vicinity of ϵ_{res} , and also such parts of T_{s-c} and T_0 are almost coincident (Fig. 16). So this change has practically no effect on the IRM results obtained above with use of the simple $G_0(\epsilon)$. So the corresponding mobility diagrams as in Fig. 12 remain also valid in the self-consistent approximation.

B. Group expansion

Next, we look for a group expansion (GE) of the self-energy matrix $\hat{\Sigma}_k(\epsilon)$ in the form

$$\hat{\Sigma}_k(\epsilon) = c\hat{T}(\epsilon)[\hat{1} + c\hat{B}_k(\epsilon) + \dots], \quad (57)$$

where the sum

$$\hat{B}_k(\epsilon) = \sum_r [e^{-ikr} \hat{A}_r(\epsilon) + \hat{A}_r^2(\epsilon)][\hat{1} - \hat{A}_r^2(\epsilon)]^{-1} \quad (58)$$

describes the effects of multiple scatterings between pairs of impurities at longitudinal distance r between them through the

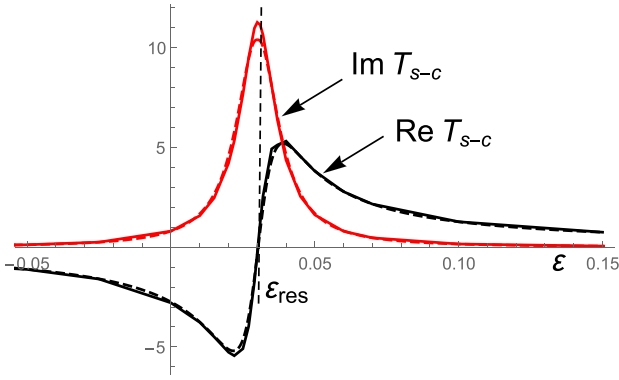


FIG. 16. Practical coincidence of self-consistent (solid lines) and simple (dashed lines) T -matrix functions for the same system as shown in Fig. 15.

related scattering matrix $\hat{A}_r(\varepsilon) = \hat{T}(\varepsilon)\hat{G}_r(\varepsilon)$ with the correlator matrix

$$\hat{G}_r(\varepsilon) = \frac{1}{4nN} \sum_{k' \neq k} e^{ik'r} \hat{G}_0(k).$$

The omitted terms on the right-hand side of Eq. (57) correspond to contributions by clusters of three and more impurities.

Notably, the important specifics of the disordered carbon NTs (and NRs), unlike the commonly studied disordered 3D or 2D crystals, consist of the following:

(i) here the longitudinal distance r between different impurities takes only discrete values; namely, $2r$ takes integer values (so the sum \sum_r can be done without the usual passing to integral $\int dr$); and

(ii) this distance can also be zero.

Thus, it can be seen from Figs. 5 and 7 that for any impurity position σ , there are $2n - 1$ other positions σ' with the same longitudinal coordinate $p_\sigma = p_{\sigma'}$. Such impurity pairs at zero longitudinal distance contribute to \hat{B}_k with

$$\hat{B}_0 = c \left(1 - \frac{1}{n}\right) [\hat{A}_0(\varepsilon) + \hat{A}_0^2(\varepsilon)] [\hat{1} - \hat{A}_0^2(\varepsilon)]^{-1}, \quad (59)$$

and this contribution results in being dominant over the resting sum $\sum_{r \neq 0}$ in Eq. (58) (see in Appendix).

Consider this in more detail for the example of ANT where all the matrices in the self-energy $\hat{\Sigma}_k$ can be substituted by scalars: $A_0(\varepsilon) = T(\varepsilon)G_0(\varepsilon)$, and $T(\varepsilon)$ can be taken in the form of Eq. (32). Then the $B_0(\varepsilon)$ contribution to GE by Eq. (57) is estimated using the explicit form of $A(\varepsilon) = \Gamma/(e - \varepsilon_{\text{res}} - i\Gamma)$ with $\Gamma = \gamma^2/(2n\sqrt{3})$ to give

$$B_0(\varepsilon) = \left(1 - \frac{1}{2n}\right) \Gamma \frac{\varepsilon - \varepsilon_{\text{res}} - i\Gamma}{(e - \varepsilon_{\text{res}})^2}. \quad (60)$$

For comparison, the lowest-degree resting term in $B_k(\varepsilon)$ is evaluated with use of the approximation for $A_r(\varepsilon)$ by Eq. (A11), as

$$\sum_{r \neq 0} e^{-ikr} A_r(\varepsilon) \approx \frac{i\Gamma \varepsilon}{4n\pi^2} \text{Li}_2(-e^{-ik/2}), \quad (61)$$

where the polylogarithmic function [34] at $k \ll 1$ is close to $\text{Li}_2(-1) = -\pi^2/12$. Thus the magnitude of the Eq. (61) term turns more than 4 orders below of that of Eq. (60) within the whole low-energy range, while the next terms in $B_k(\varepsilon)$ end up being yet much smaller.

Then, taking the GE convergence criterion as $c|B_0(\varepsilon)| < 1$, the T -matrix validity condition ends up being from Eq. (60) well approximated by

$$|\varepsilon - \varepsilon_{\text{res}}| \gtrsim \Gamma\sqrt{c}, \quad (62)$$

and it can only fail in a very narrow vicinity of ε_{res} (the blue range in Fig. 12 for ZNT) deeply within the localized range, just confirming localization of states there. In a similar way, this conclusion can be reached for other nanosystems considered here, justifying the above obtained pictures of spectrum restructuring in them.

IX. DISCUSSION OF RESULTS

The above obtained results on restructured low-energy quasiparticle spectra in carbon nanosystems can be discussed in the context of disordered 1D crystalline systems generally known not to contain conducting states at any degree of disorder [36–40]. But their presence in the disordered NTs and NRs indicates again the principal qualitative difference of these structures from the strictly 1D chains. Besides the above noted possibility for zero longitudinal distance between different impurity positions, it can be yet illustrated by the behaviors of correlator functions with growing interimpurity distance r : converging as $\sim 1/r^2$ by Eq. (A11) for NTs and diverging as $\sim 1/r$ for really 1D chains [as that by single $g_r(\varepsilon)$ by Eq. (A9)], making the related GE divergent at all energies. So we can conclude that it is just the presence of additional transversal degrees of freedom in quasi-1D systems that enables their conductivity under disorder [41–43].

The found intermittence of conducting and localized energy ranges in the considered nanosystems can be then used for their various practical applications. Thus, the most straightforward effects are expected in frequency ω - and temperature T -dependent electric conductivity, following from the general Kubo-Greenwood formula [44,45] presented here in the form

$$\begin{aligned} \sigma(\omega, T) &= \frac{e^2}{\pi} \int d\varepsilon \frac{f(\varepsilon, T) - f(\varepsilon', T)}{\omega} \\ &\times \int_{\text{cond}} dk v_k(\varepsilon) v_k(\varepsilon') \text{Im}G_k(\varepsilon) \text{Im}G_k(\varepsilon'). \end{aligned} \quad (63)$$

It includes the Fermi function $f(\varepsilon, T) = [e^{(\varepsilon - \varepsilon_F)/T} + 1]^{-1}$, the group velocity $v_k(\varepsilon) = [\partial k_\varepsilon / \partial \varepsilon]^{-1}$, the ac shifted energy $\varepsilon' = \varepsilon + \hbar\omega$, and the integration \int_{cond} avoids localized ranges (as those shadowed in Fig. 11).

First of all, consider the simplest dc limit:

$$\lim_{\omega \rightarrow 0} \frac{f(\varepsilon, T) - f(\varepsilon', T)}{\omega} \rightarrow \frac{1}{4T \text{Cosh}^2[(\varepsilon - \varepsilon_F)/2T]},$$

which then goes to $\delta(\varepsilon - \varepsilon_F)$ at $T \rightarrow 0$, defining

$$\sigma(0, 0) = \frac{e^2}{\pi} \int_{\text{cond}} dk v_k^2(\varepsilon_F) [\text{Im}G_k(\varepsilon_F)]^2,$$

and this becomes zero for ε_F laying within a localized range. But such insulating state can be converted to conducting by applying quite a small external gate voltage V_g . Thus, for the ANT case of Fig. 11, the initial $\varepsilon_F \approx \varepsilon_{\text{res}} = 0.03$ (in units of $t \approx 2.8$ eV) could reach the nearest mobility edges with gating either ≈ 100 meV upward or ≈ 80 meV downward, and the resulting reversible insulator-metal transitions should stay well resolved up to room temperatures.

Otherwise, a quite sharp threshold in optical conductivity can be reached by applying IR radiation of ~ 10 THz (which may be also combined with a slight gate tuning $V_g \sim 5$ meV). A more detailed description of the $\sigma(\omega, T)$ behavior readily follows from the above given T -matrix solutions for $v_k(\varepsilon)$ and $\text{Im}G_k(\varepsilon)$. All these effects are most diversified with formation of multiple mobility edges (above the second critical concentration c_1).

The above quantitative results were delimited to a single choice of Cu impurity in its top position over a host carbon atom, but they can be readily extended to other impurities in different positions, providing a variety of possible values for the relevant ε_{res} and γ parameters and so a much broader field of resulting electronic dynamics. Nevertheless, their qualitative features indicated in the present study should stay proper for all of them.

Yet another practical condition for validity of the above conclusions consists in that a NT (or a NR) should be long enough compared to the localization length l_{loc} of quasiparticle states near the mobility edges. The latter can be estimated as $l_{\text{loc}} \sim v_{k_j} \tau(\varepsilon_j)$ using Eqs. (31), (32), and (45) for j th mobility edge which results in $l_{\text{loc}} \sim 1/\Gamma$. Thus for the same instance of ANT with $n = 12$ we obtain numerically $l_{\text{loc}} \sim 400$ nm; therefore such a NT should extend to more than ~ 5 μm in length.

At least, it should be especially noted that, in accordance with the reasoning in Sec. VII, the highest sensibility of NT structures to impurity perturbations and the richest variety of resulting intermittent conductive and localized spectrum ranges in them are expected in the properly designed TNTs at a proper choice of impurity centers and their concentrations.

ACKNOWLEDGMENTS

The authors are thankful to L. S. Brizhik, A. A. Eremko, and S. G. Sharapov for their attention to this work and its valuable discussion. V.L. acknowledges the partial support of his work by the Simons Foundation Grant No. 1290587.

APPENDIX: LOCATOR AND CORRELATOR

We calculate the integral that contributes to the locator GF in a 1D nanosystem, for an example of ε_k mode in ANT,

$$g(\varepsilon) = \frac{1}{4\pi} \int_{-2\pi}^{2\pi} \frac{dk}{\varepsilon - 1 + 2 \cos \frac{k}{2}}, \quad (\text{A1})$$

valid at $-3 < \varepsilon < 1$. By the common change of variable, $t = \tan \frac{k}{4}$, this integral is rewritten as

$$g(\varepsilon) = \frac{1}{\pi} \int_{-\infty}^{\infty} \frac{dt}{1 + \varepsilon - (3 - \varepsilon)t^2}, \quad (\text{A2})$$

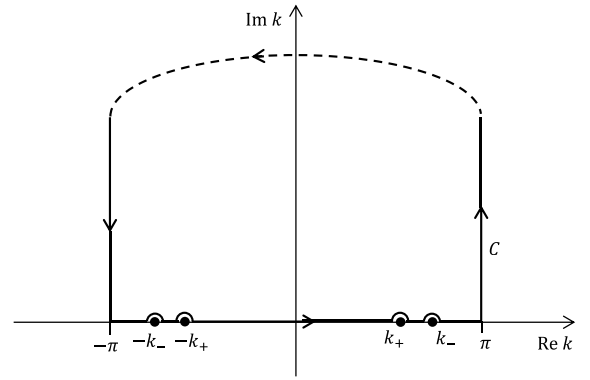


FIG. 17. Integration contour for Eq. (A8).

giving the explicit result

$$g(\varepsilon) = i \frac{\theta(1 + \varepsilon)\theta(3 - \varepsilon)}{\sqrt{(3 - \varepsilon)(1 + \varepsilon)}}, \quad (\text{A3})$$

with the standard θ functions delimiting the ε_k energy range.

Another contribution to $G_0(\varepsilon)$ from $-\varepsilon_k$ mode, valid at $-1 < \varepsilon < 3$, is

$$g(-\varepsilon) = i \frac{\theta(1 - \varepsilon)\theta(3 + \varepsilon)}{\sqrt{(3 + \varepsilon)(1 - \varepsilon)}}, \quad (\text{A4})$$

which then enters the full expression for locator GF:

$$G_0(\varepsilon) = \frac{g(\varepsilon) - g(-\varepsilon)}{4n}. \quad (\text{A5})$$

The next step is to calculate, for the same ANT, the correlator between a pair of impurities at distance r ,

$$G_r(\varepsilon) = \frac{g_r(\varepsilon) - g_r(-\varepsilon)}{4n}, \quad (\text{A6})$$

through the integral

$$g_r(\varepsilon) = \frac{1}{4\pi} \int_{-2\pi}^{2\pi} f_r(k, \varepsilon) dk, \quad (\text{A7})$$

with its integrand

$$f_r(k, \varepsilon) = \frac{e^{ikr}}{\varepsilon - 1 + 2 \cos \frac{k}{2}},$$

especially considering long distances, $r \gg 1$. It can be done passing to the contour integral,

$$\int_C f_r(k, \varepsilon) dk = g_r(\varepsilon) + \int_0^\infty [f_r(2\pi + iy, \varepsilon) - f_r(-2\pi + iy, \varepsilon)] dy = 0, \quad (\text{A8})$$

where the contour C in the complex momentum plane (Fig. 17) includes the $f_r(k, \varepsilon)$ poles:

$$\pm k_\varepsilon = \pm 2 \arccos \frac{1 - \varepsilon}{2}.$$

For integration along the imaginary axis we use the relations $\cos(\pm\pi + iy/2) = -\cosh(y/2)$ and $e^{i(\pm 2\pi + iy)r} = (-1)^{2r} e^{-yr}$ (noting that the longitudinal distance r between

impurities takes here only integer or half-integer values) and the explicit formula

$$I_{2r}(b) = \int_0^\infty \frac{e^{-2ry} dy}{\cosh y + b} = \frac{1}{2r+1} \left[\left(\frac{b}{\sqrt{b^2-1}} + 1 \right) \times {}_2F_1 \left(1, 2r+1; 2r+2; \frac{1}{\sqrt{b^2-1}-b} \right) + \left(\frac{b}{\sqrt{b^2-1}} - 1 \right) \times {}_2F_1 \left(1, 2r+1; 2r+2; -\frac{1}{\sqrt{b^2-1}+b} \right) \right], \quad (\text{A9})$$

where ${}_2F_1(n, m; p; q)$ is the hypergeometric function [46]. Then the sought correlator follows from Eqs. (A6), (A7), and (A9) analytically as

$$G_r(\varepsilon) = \frac{(-1)^{2r}}{16\pi n} [I_{2r-1}(b_\varepsilon) - I_{2r+1}(b_\varepsilon) - I_{2r-1}(b_{-\varepsilon}) + I_{2r+1}(b_{-\varepsilon})] \quad (\text{A10})$$

with the energy-dependent parameter

$$b_\varepsilon = \frac{1-\varepsilon}{2}.$$

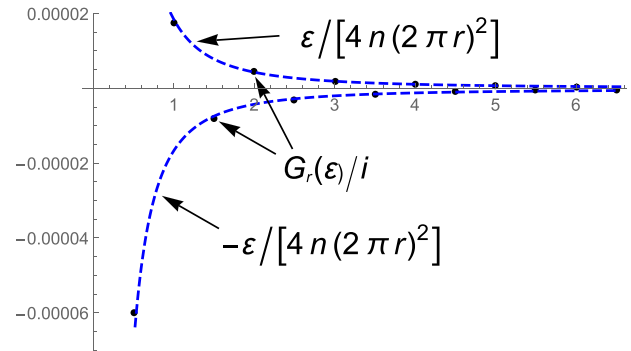


FIG. 18. Exact discrete values of the correlator $G_r(\varepsilon)$ by Eq. (A10) (solid points) and their approximation by Eq. (A11) (dashed curves) for the choice of $\varepsilon = \varepsilon_{\text{res}}$ and $n = 12$.

Notably, the full form by Eq. (A10) admits a very simple approximation:

$$G_r(\varepsilon) \approx i \frac{(-1)^{2r} \varepsilon}{4n(2\pi r)^2}, \quad (\text{A11})$$

however quite precise at all nonzero interimpurity distances (see Fig. 18) and suitable for detailed evaluations as in analysis of particular GE terms (Sec. VIII B).

- [1] K. S. Novoselov, A. K. Geim, S. V. Morozov, D. Jiang, Y. Zhang, S. V. Dubonos, I. V. Grigorieva, and A. A. Firsov, *Science* **306**, 666 (2004).
- [2] S. V. Morozov, K. S. Novoselov, F. Schedin, D. Jiang, A. A. Firsov, and A. K. Geim, *Phys. Rev. B* **72**, 201401(R) (2005).
- [3] A. H. Castro Neto, F. Guinea, N. M. R. Peres, K. S. Novoselov, and A. K. Geim, *Rev. Mod. Phys.* **81**, 109 (2009).
- [4] D. Tománek, *Guide through the Nanocarbon Jungle* (Morgan and Claypool Publishers, New York, 2014).
- [5] M. Inagaki and F. Kang, *J. Mater. Chem. A* **2**, 13193 (2014).
- [6] M. I. Katsnelson, *Graphene: Carbon in Two Dimensions* (Cambridge University Press, Cambridge, 2012).
- [7] K. Wakabayashi, K. Sasaki, T. Nakanishi, and T. Enoki, *Sci. Technol. Adv. Mater.* **11**, 054504 (2010).
- [8] S. Iijima, *Phys. B: Condens. Matter* **323**, 1 (2002).
- [9] J.-C. Charlier, X. Blase, and S. Roche, *Rev. Mod. Phys.* **79**, 677 (2007).
- [10] A. H. Nevidomskyy, G. Csányi, and M. C. Payne, *Phys. Rev. Lett.* **91**, 105502 (2003).
- [11] S. Jalili, M. Jafari, and J. Habibian, *J. Iranian Chem. Soc.* **5**, 641 (2008).
- [12] M. Pumera, A. Ambrosia, and E. Lay Khim Chnga, *Chem. Sci.* **3**, 3347 (2012).
- [13] Y. V. Skrypnik and V. M. Loktev, *Low Temp. Phys.* **44**, 1112 (2018).
- [14] J. Vejpravova, B. Pacakova, and M. Kalbac, *Analyst* **141**, 2639 (2016).
- [15] T. O. Wehling, M. I. Katsnelson, and A. I. Lichtenstein, *Phys. Rev. B* **80**, 085428 (2009).
- [16] P. T. Araujo, M. Terrones, and M. S. Dresselhaus, *Mater. Today* **15**, 98 (2012).
- [17] M. Fujita, K. Wakabayashi, K. Nakada, and K. Kusakabe, *J. Phys. Soc. Jpn.* **65**, 1920 (1996).
- [18] Y. G. Pogorelov, D. Kochan, and V. M. Loktev, *Low Temp. Phys.* **47**, 754 (2021).
- [19] Y. G. Pogorelov and V. M. Loktev, *Phys. Rev. B* **106**, 224202 (2022).
- [20] P. R. Wallace, *Phys. Rev.* **71**, 622 (1947).
- [21] K. Nakada, M. Fujita, G. Dresselhaus, and M. S. Dresselhaus, *Phys. Rev. B* **54**, 17954 (1996).
- [22] I. M. Lifshitz, *Adv. Phys.* **13**, 483 (1964).
- [23] P. W. Anderson, *Phys. Rev.* **124**, 41 (1961).
- [24] D. Zubarev, *Sov. Phys. Usp.* **3**, 320 (1960).
- [25] E. N. Economou, *Green's Functions in Quantum Physics* (Springer, Berlin, 1979).
- [26] S. Irmer, D. Kochan, J. Lee, and J. Fabian, *Phys. Rev. B* **97**, 075417 (2018).
- [27] M. A. Ivanov, V. M. Loktev, and Y. G. Pogorelov, *Phys. Rep.* **153**, 209 (1987).
- [28] V. M. Loktev and Yu. G. Pogorelov, *Dopants and Impurities in High-T_c Superconductors* (Akademperiodyka, Kyiv, 2015).
- [29] Y. G. Pogorelov, V. M. Loktev, and D. Kochan, *Phys. Rev. B* **102**, 155414 (2020).
- [30] V. L. Bonch-Bruевич and S. V. Tyablikov, *The Green Function Method in Statistical Mechanics* (North Holland Publishing House, Amsterdam, 1962).
- [31] A. F. Ioffe and A. R. Regel, *Prog. Semicond.* **4**, 237 (1960).
- [32] N. F. Mott, *Philos. Mag.* **19**, 835 (1969).
- [33] K. F. Freed, *Phys. Rev. B* **5**, 4802 (1972).
- [34] M. Abramowitz and I. Stegun, *Handbook of Mathematical Functions with Formulas, Graphs, and Mathematical Tables* (Dover Publications, New York, 1972).

- [35] C. L. Kane and E. J. Mele, *Phys. Rev. Lett.* **78**, 1932 (1997).
- [36] P. W. Anderson, *Phys. Rev.* **109**, 1492 (1958).
- [37] M. Hjort and S. Stafström, *Phys. Rev. B* **62**, 5245 (2000).
- [38] D. Delande, K. Sacha, M. Plodzień, S. K. Avazbaev, and J. Zakrzewski, *New J. Phys.* **15**, 045021 (2013).
- [39] R. Vosk, D. A. Huse, and E. Altman, *Phys. Rev. X* **5**, 031032 (2015).
- [40] Y. Tao, *Phys. Lett. A* **455**, 128517 (2022).
- [41] T. Ando and T. Nakanishi, *J. Phys. Soc. Jpn.* **67**, 1704 (1998).
- [42] T. Ando, *Semicond. Sci. Technol.* **15**, R13 (2000).
- [43] B. Biel, X. Blase, F. Triozon, and S. Roche, *Phys. Rev. Lett.* **102**, 096803 (2009).
- [44] R. Kubo, *J. Phys. Soc. Jpn.* **12**, 570 (1957).
- [45] D. A. Greenwood, *Proc. Phys. Soc.* **71**, 585 (1958).
- [46] G. E. Andrews, R. Askey, and R. Roy, *Special Functions*, Encyclopedia of Mathematics and its Applications, Vol. 71 (Cambridge University Press, Cambridge, 1999).